



1 The NUIST Earth System Model (NESM) version 3:

2 Description and preliminary evaluation

3

4 Cao, Jian^{1,2}, Bin Wang^{1,2,*}, Young-Min Yang², Libin Ma^{1,2}, Juan Li^{1,2}, Bo Sun^{1,2}, Yan

5 Bao^{1,2}, Jie He^{1,2} and Xiao Zhou²

6 1. Earth System Modeling Center, the Nanjing University of Information Science and

7 Technology, Nanjing 210044, China

8 2. China-US joint Atmosphere-Ocean Research Center and International Pacific Research

9 Center, University of Hawaii, Honolulu Hawaii 96822 USA

10

11

12

13

14 *Corresponding author: Bin Wang, wangbin@hawaii.edu

15

16

17



18

Abstract

19 The Nanjing University of Information Science and Technology Earth System Model
20 version 3 (NESM v3) has been developed, aiming to provide a numerical modeling
21 platform for cross-disciplinary earth system studies, project future Earth's climate and
22 environment changes, as well conduct subseasonal-to-seasonal prediction. While the
23 previous model version NESM v1 simulates well the internal modes of climate variability,
24 it has no vegetation dynamics and suffers considerable radiative energy imbalance at the
25 top of the atmosphere and surface, resulting in large biases in the global mean surface air
26 temperature, which limit its utility to simulate past and project future climate changes.
27 The NESM v3 upgraded the atmospheric and land surface model components and
28 improved physical parameterization and conservation of coupling variables. Here we
29 describe the new version's basic features and how the major improvements were made.
30 We demonstrate the v3 model's fidelity and suitability to address the global climate
31 variability and change issues. The 500-year PI experiment shows negligible trends in the
32 net heat flux at the top of atmosphere and the Earth surface. Consistently, the simulated
33 global mean surface air temperature, land surface temperature and sea surface
34 temperature (SST) are all in a quasi-equilibrium state. The conservation of global water is
35 demonstrated by the stable evolution of the global mean precipitation, sea surface salinity
36 (SSS) and sea water salinity. The sea ice extents (SIEs), as a major indication of high
37 latitude climate, also maintain a balanced state. The simulated spatial patterns of the
38 mean outgoing longwave radiation, SST, precipitation, SSS fields are realistic, but the
39 model suffers from a cold bias in the North Atlantic, a warm bias in the Southern Ocean
40 and associated deficient Antarctic sea ice area, as well as a delicate sign of the double



41 ITCZ syndrome. The estimate radiative forcing of quadrupling carbon dioxide is about
42 7.24 Wm^{-2} , yielding a climate sensitivity feedback parameter of $-0.98 \text{ Wm}^{-2} \text{ K}^{-1}$, and the
43 equilibrium climate sensitivity is 3.69K. The transient climate response from the
44 1pct/year increasing CO_2 experiment is 2.16K. The model's performance on internal
45 modes and responses to external forcing during the historical period will be documented
46 in an accompanying paper.

47

48 **1. Introduction**

49 Large internal variability of the Earth climate system involves complex feedbacks
50 among the atmosphere, hydrosphere, cryosphere, land surface and biosphere. As an
51 essential tool to reproduce the Earth's paleoclimate evolution, project future climate
52 change, and understand the mechanisms governing climate variability and change, the
53 Climate system model (CSM) and Earth System Model (ESM) have attracted greatest
54 attention of the scientific community. Starting from 1995, the World Climate Research
55 Project (WCRP) established and regularly organized Coupled Model Intercomparison
56 Projects (CMIPs) (Meehl et al. 2000). The CMIP has not only stimulated the coupled
57 model development, facilitated model output validation, deepened scientific
58 understanding of the Earth climate change, but also provided scientific guidance for the
59 Intergovernmental Panel on Climate Change (IPCC).

60 The first generation of Nanjing University Information Science and Technology
61 (NUIST) Earth System Model (NESM v1, Cao et al 2015) was established with the
62 atmospheric model ECHAM v5.3, ocean model NEMO v3.4, sea ice model CICE v4.1



63 and coupler 3 of the Ocean-Atmosphere-Sea-Ice-Soil Model Coupling Toolkit
64 (OASIS3.0-MCT). It was targeted to meet the demand of seamless climate prediction,
65 simulate the past and project future climate change, and study of climate variability of
66 high-impact weather events. The performances of NESM v1 model have been evaluated
67 (Cao et al. 2015) and further developed into a seasonal prediction system (NESM v2).
68 The NESM v1 was also used to study the changes in Last Glacial Maximum climate and
69 global monsoon, demonstrating reasonable model response with external forcing (Cao et
70 al. 2016). Numerical experiments with NESM v2 were conducted to confirm the sources
71 of predictability of the Indian summer monsoon rainfall (Li et al. 2016) and the winter
72 extremely cold days in East Asia (Luo and Wang submitted).

73 However, the previous model versions have no vegetation dynamics in the land
74 surface model and cannot be used to study carbon cycle; and the response of the coupled
75 system to carbon dioxide forcing was over-sensitive. Another serious problem is the
76 relatively large energy imbalance at the TOA and surface, both have an imbalance of
77 $\sim 2\text{Wm}^{-2}$. There are also significant biases in the TOA net solar radiation and OLR.
78 Meanwhile, the poorly resolved vertical layers prevented correct simulation of
79 stratosphere phenomena as well as high-level jet stream. They have large land surface
80 temperature biases and a severe double ITCZ syndrome. The SST over high latitude
81 North Atlantic is excessively cold, the strength and extent of the Atlantic Meridional
82 Overturning Circulation (AMOC) is underestimated, the Southern Ocean is too warm,
83 and the sea ice coverage over the Antarctic is substantially deficient.

84 Facing the forth coming CMIP6, a more comprehensive and improved Earth System
85 Model is needed to perform CMIP6 experiments and to address forcing-related scientific



86 questions. For this purpose, we have developed a new version of NESM v3.0. The major
87 changes include an updated land surface model with dynamic vegetation and carbon
88 exchange, improved shortwave and longwave radiation schemes, new schemes for
89 description of aerosols and computation of surface albedo, increased vertical resolution of
90 the atmosphere model and horizontal resolution of the ocean and sea ice models.

91 As a registered model of CMIP6, the NESMv3.0 model is to be used to perform the
92 DECK simulation, historical experiment, and some endorsed MIPs following the CMIP6
93 experiment design protocol (Eyring et al. 2016). The selected MIPs include: Detection
94 and Attribution Model Intercomparison Project (DAMIP), Scenario Model
95 Intercomparison Project (ScenarioMIP), Decadal Climate Prediction Project (DCPP),
96 Global Monsoons Model Intercomparison Project (GMMIP), Paleoclimate Modelling
97 Intercomparison Project (PMIP), Volcanic Forcings Model Intercomparison Project
98 (VolMIP), and Geoengineering Model Intercomparison Project (GeoMIP).

99 This paper documents the main features of the NESM v3, the major model
100 improvement, and the preliminary evaluation of model's long term integration and
101 climate sensitivity to carbon dioxide forcing. In the new version 3, the energy balance is
102 substantially improved, including the net shortwave radiation and outgoing longwave
103 radiation and their balance. The biases are in a few tenths Wm^{-2} and the trends are
104 negligible. This is demonstrated by the PI experiment with perpetual unchanged forcing,
105 and the climate sensitivity is tested through the abruptly quadrupling CO_2 experiment and
106 gradually 1% CO_2 /year increase experiment.



107 The model description is presented in Section 2, which is followed by the coupled
108 model tuning strategy (Section 3). In Section 4 and 5, the model long-term stability and
109 the mean climate states are evaluated. Section 6 examines the model climate sensitivity in
110 perturbing atmospheric carbon dioxide concentration. The last section presents a
111 summary.

112 **2. Model description and validation data**

113 The NESM v3 consists of the ECHAM v6.3 atmospheric model, which directly
114 coupled with JSBACH land surface model, the NEMO v3.4 ocean model, the CICE v4.1
115 sea ice model; and the OASIS3-MCT_3.0 coupler. The model structure is illustrated in
116 Fig.1, and brief description of each component model follows.

117 **2.1 Atmosphere and land surface model**

118 The ECHAM v6.3 and JSBACH model are originally adopted from the Max Planck
119 Institute ECHAM serial model. A brief introduction will be presented here; the detailed
120 documentation can be found in Stevens et al. (2012) and Giorgetta et al. (2013). The
121 ECHAM v6.3 employs the spectral/finite-difference dynamic core for adiabatic process.
122 Calculations of all parameterizations and non-linear terms are transferred to Gaussian
123 grids. A hybrid sigma-pressure coordinate system (Simmons et al. 1999) is used in the
124 vertical discretization. The shortwave and longwave radiation schemes are both from the
125 Rapid Radiation Transfer Model for General Circulation model's (RRTM-G) scheme
126 (Iacono et al. 2008), which takes the two-stream approach. The upward and downward
127 irradiance are calculated over a predetermined number of pseudo wavelengths. The time
128 step for radiation scheme is two hours. The turbulent transport employs the turbulent



129 kinetic energy scheme, and the surface fluxes are calculated using the bulk-exchange
130 formula which is based on Monin-Obukhov similarity theory. The model parameterizes
131 shallow, deep and midlevel convection separately. The deep convection is based on mass-
132 flux framework developed by Tiedtke (1989) and further improved by Nordeng (1994).
133 Currently, the shallow, deep and midlevel convection are parameterized by the Tiedtke,
134 Nordeng, and Tiedtke scheme, respectively. The stratiform cloud scheme contains the
135 prognostic equations for the vapor, liquid, and ice phase, respectively, a cloud
136 microphysical scheme, and a diagnostic cloud cover scheme. The ECHAM v6.3
137 implements the Subgrid Scale Orographic Parameterization scheme (Lott and Miller 1997,
138 Lott 1999) to represent the momentum transport arising from subgrid orograph.

139 The JSBASH land surface model simulates fluxes of energy, momentum, moisture,
140 and tracer gases between the land surface and atmosphere (Raddatz et al. 2007). The
141 JSBACH model contains a 5-layer soil, a dynamic vegetation scheme and a land albedo
142 scheme. The tiled structure of land surface is divided into eight natural Plant Functional
143 Types (PFTs), four anthropogenic PFTs and two types of bare surface (Brovkin et al. 2013).
144 The dynamic vegetation scheme is based on the assumption that the competition between
145 different PFTs is determined by their relative competitiveness expressed in the annual net
146 primary productivity, as well as natural and disturbance-driven mortality. The surface
147 albedo is calculated at each tile of the land surface for near-infrared and visible range of
148 solar radiation.

149 **2.2 Ocean model**



150 The ocean component model of NESMv3 is Ocean PARallelise (OPA), the ocean part
151 of NEMO v3.4 (Nucleus of European Modelling of the Ocean). The primitive equation of
152 ocean model is numerically solved on an orthogonal curvilinear grid. It uses the isotropic
153 Mercator south of 20°N, and a stretched grid north of 20°N with two poles in Canada and
154 Siberia, which removes the singularity of spherical coordinate in the Arctic ocean and
155 allows the cross polar flow (Madec and Imbard, 1996). The ORCA1 configuration of
156 ocean model corresponds to a resolution of 1 degree of longitude and a variable mesh of
157 1/3 to 1 degree of latitudes from the equator to pole. It has 46 vertical layers which adopts
158 the z-coordinate with partial steps (Adcroft et al., 1997; Bernard et al., 2006). At the
159 ocean surface, the linear free surface method is used (Roullet and Madec, 2000).
160 Advection of tracer uses the total variance dissipations scheme (TVD) (Zalesak, 1979).
161 Horizontal momentum is diffused with a Laplacian operator and 2-D spatially-varying
162 kinematic viscosity coefficient. The vertical mixing of tracer and momentum is
163 parameterized using turbulent kinetic energy scheme. Besides, the lateral diffusion is
164 solved on the neutral direction (Redi, 1982) and includes eddy-induced advective
165 processes (Gent and McWilliams, 1990). The incoming solar radiation is distributed in
166 the surface layers of the ocean using simplified RGB and chlorophyll-dependent
167 attenuation parameters (Lengaigne et al., 2009). The model uses a diffusive bottom
168 boundary layer (Bechmann and Doscher 1997).

169 **2.3 Sea ice model**

170 The sea ice model in the NESM v3 is CICE v4.1, which is originally developed at the
171 Los Almos National Laboratory. The model solves dynamic and thermodynamic
172 equations for five categories of ice thickness. The lower bound for the five thickness



173 categories are 0, 0.6, 1.4, 2.4, and 3.6m. The sea ice deformation is computed basing on
174 the Elastic-Viscous-Plastic scheme (Hunck and Dukowicz 2002) with the ice strength
175 determined by using the formulation of Rothrock (1975). The ice thermodynamics are
176 calculated at five ice layers corresponding to each thickness category instead of zero-
177 layer thermodynamic option.

178 **2.4 Coupling method with OASIS3-MCT**

179 The coupling method is the same as the previous version of NESM v1, and the detail
180 information is described in Cao et al (2015). But the coupler has been upgraded from
181 OASIS3-MCT to OASIS3-MCT_3.0 (Valcke and Coquart 2015), which is a fully
182 parallelized tool for coupled model. The coupler is used to synchronize, interpolate and
183 exchange the coupling fields among the atmospheric, oceanic and sea ice component
184 models. To conserve the exchange coupling fields, the second order conservation
185 interpolation is used in remapping the energy, mass, momentum, and tracers, so to avoid
186 energy, momentum loss and spurious climate drift. The component models are coupled
187 daily.

188 **2.5 Configuration**

189 Two subversions are included in the NESM v3, namely the standard-resolution version
190 (sr) and low-resolution (lr) version. In the atmospheric model, the sr and lr versions have
191 a horizontal resolution of T63 and T31, respectively. The T63 corresponds to about 1.9°
192 in meridional and zonal directions. The sr (lr) version has 47 (31) levels in the vertical
193 which extends from the surface up to 0.01 (1.0) hPa. The resolution of land surface model
194 is the same as the atmospheric model. The resolution of ocean model is higher than



195 atmospheric model with the longitudinal resolution of $1^\circ \times 1^\circ$ in sr and $2^\circ \times 2^\circ$ in lr
196 version. The resolution in the meridional direction is refined to $1/3^\circ$ and $2/3^\circ$,
197 respectively, over the tropical region. In the vertical direction, the sr (lr) version has 46
198 (31) vertical layers with the first 15 (9) layers at the top 100 meters. In both sr and lr
199 versions, the sea ice model resolution is about $1^\circ \times 1/2^\circ$ in meridional and zonal directions
200 with four sea ice layers and one snow layer on the top of the ice surface.

201 **2.6 Validation data**

202 To validate the model performance, the following observational data are used: (1) the
203 combined precipitation data of Global Precipitation Climatology Project (GPCP) version
204 2.2 and Climate Prediction Center Merged Analysis of Precipitation (CMAP) (Xie and
205 Arkin, 1997; Lee and Wang, 2014); (2) Hadley Centre Global Sea Ice and Sea Surface
206 Temperature (HadISST), (Rayner et al., 2003); (3) Clouds and the Earth's Radiant
207 Energy System- Energy Balanced and Filled (CERES-EBAF, Loeb et al. 2009); (4)
208 World Ocean Atlas 2009 (WOA09) (Locarnini et al. 2010).

209 **3. Model improvement and tuning**

210 Model sub-grid processes are represented by physical parameterizations.
211 Improvement of physical parametrizations and calibration the parameters within the
212 parametrization schemes using constraints obtained from observation, physical
213 understanding or empirical estimation is an integral part of the model development cycle.
214 Our strategy to improve model performance and tuning parameters includes three
215 elements. First, our principle is that the final tuning of all parameters must be conducted
216 using the fully coupled climate model. Second, to efficiently identify the model's



217 weakness and the effects of the tuning, we designed a standard metrics for evaluation of
218 the model's climatology and major modes of variability, which include total of 160 fields
219 covering the climatology of the atmosphere, ocean, land and sea ice, and internal and
220 coupled modes of variability such as Madden-Julian oscillation (MJO), Arctic oscillation
221 (AO), Antarctic Oscillation (AAO), North Atlantic Oscillation (NAO), global monsoon,
222 El Nino-Southern Oscillation (ENSO), Atlantic Meridional Overturning Circulation
223 (AMOC), Atlantic multidecadal Oscillation (AMO), Pacific Decadal Oscillation (PDO),
224 and major teleconnection patterns etc. Result from each tuning experiment is compared
225 with the corresponding observations when they are available or CMIP5 multi-model
226 ensemble means when observations are not available. This assessment process helps to
227 identify the models' major problems and the consequences of the tuning, and to
228 understand how the tuning works. Third, a low-resolution version model, the NESM v3lr,
229 is developed, which allows integration about four times faster than the standard
230 resolution version so that the tuning experiments can get results quickly. Once the tuning
231 is successful in the low-resolution model, similar tuning is applied to the standard
232 resolution version with necessary resolution-dependent adjustment.

233 The initial version of the v3 model has considerable trends in the surface air
234 temperature and SST, which is associated with the reduced net solar radiation and OLR,
235 as well as a large energy imbalance at the top of the atmosphere (TOA). The global mean
236 surface air temperature (TAS) and SST was about 1 K lower than the observed and
237 suffered a continuing drift. Meanwhile, the sea ice extent and sea ice thickness in both
238 Hemispheres kept increasing in the long-term integration. Our first task was aimed at
239 obtaining a nearly balanced global mean energy at the TOA and surface, as well as a



240 reasonable global mean surface temperature with perpetual pre-industry forcing. This is
241 critical for achieving a stable long-term integration in pre-industry simulation which acts
242 as the benchmark experiment for entry card for CMIP6 (DECK) and historical run as well
243 as some other MIPs. Another tuning consideration is the long-term climatology and
244 internal modes of the Earth System in the current climate condition. Efforts are made to
245 minimize the biases in the simulated SST, sea level pressure (SLP), precipitation, zonal
246 mean temperature and wind, ocean mean state (sea surface salinity, mix layer depth etc.)
247 as well as ENSO, global monsoon, and MJO. In addition, the historical evolution of
248 surface temperature is an important measurement of the model's fidelity. This is along
249 with the abrupt quadrupling and gradually increased $1\%yr^{-1}$ CO₂ experiments in
250 estimating the model climate sensitivity.

251 The key tuning parameters in the v3 versions are related to the stratiform cloud,
252 cumulus convection, ocean mixing process, and sea ice albedos. Iterative tunings were
253 conducted in the standalone component models with observed/reanalysis forcing and in
254 the coupled model during the PI control run. To achieve a better global mean radiative
255 energy level and a near zero (within a few tenth $W m^{-2}$) net global mean heat flux budget,
256 the parameter calibrations are conducted on the relative humidity threshold that is related
257 to cloud forming process and the estimated cloud cover (Mauritsen et al. 2012). The
258 parameters involved in the cloud microphysics are also tuned, including the accretion of
259 cloud water (ice) to rain (snow), auto-conversion rate of cloud water to rain, and ice
260 crystal and rain drop fall speeds, which are recognized as effective parameters in
261 affecting both short and longwave radiation (Mauritsen et al. 2012, Hourdin et al. 2017).



262 Even with reasonable global mean SST, the model simulated excessive sea ice extent
263 over the Arctic, especially over the Davis Strait, Fram Strait and North Atlantic during
264 winter. The export of sea ice from Davis Strait significantly increases the SST and
265 salinity biases. To mitigate the North Hemisphere sea ice extent bias, the sea ice albedo
266 and ice transport-related parameters were adjusted. Sea ice albedo is one of the most
267 effective tunable parameter to adjust sea ice extent and thickness (Hunke 2010). The
268 default sea ice albedo parameterization takes into account the radiative spectral band, ice
269 thickness and others. The visible and near-infrared albedos are set to 0.73, 0.31 for ice
270 greater than 0.3m, and the corresponding cold snow albedos are 0.93 and 0.65,
271 respectively. Those values are slightly smaller than the corresponding default
272 configurations. On the other hand, the sea ice motion is largely driven by the ocean
273 currents, sea surface height gradients and wind stress. The efficiencies of air-ice and
274 ocean-ice drag are important for sea ice transport, as well as sea ice extent during winter
275 and spring (Urrego-Blanco et al. 2016). In this model, the ice surface roughness was
276 decreased and the ocean-ice drag coefficient was increased to decrease the sea ice export
277 over Davis and Fram Strait. This is based on the understanding that the air-ice and ocean-
278 ice drag parametrizations have large uncertainty in the current CICE model.

279 Concerning the internal modes, ENSO and Intraseasonal oscillation (ISO) are
280 recognized as the dominate modes on the interannual and intraseasonal time scale,
281 respectively. They significantly influence the tropical and global climate through
282 atmospheric teleconnections. Much attention was paid to improve the simulation of
283 ENSO and ISO in v3.



284 The ENSO-related SST variability, ENSO phase locking to annual cycle, and the
285 equatorial Pacific cold SST bias are closely related (Ham and Kug 2014). CMIP5 models'
286 results suggested that the models having less cold tongue SST bias reproduce more
287 realistic ENSO phase locking owing to models' simulation of more realistic coupled
288 feedbacks. The change of cloud parametrization has an effect on the mitigation of the
289 cold tongue SST bias, which can lead to an improved ENSO phase locking (Wengel. et al.
290 2017). In the NESM v3 model, the parameter of deep convective entrainment and
291 convective mass flux above the buoyance layer have been increased which resulted in a
292 reduced cold tongue bias and zonal wind stress over the equatorial Eastern Pacific,
293 removal of the excessive SST variance over the central Pacific, and improved ENSO
294 phase locking.

295 The entrainments in deep and shallow convections are associated with the moisture
296 supply in the free atmosphere. Strong convection plumes can increase the water supply
297 for the formation of stratiform clouds, leading to an increase of stratiform precipitation.
298 The interaction between wave dynamics and precipitation heating is essential for the
299 development and propagation of intraseasonal oscillation (Fu and Wang 2009). The
300 entrainment rates associated with convections are adjusted which allow more stratiform
301 precipitation formed in the coupled model. It strengthens the ISO signal and also
302 significantly enhances the MJO eastward propagation.

303 **4. Model stability under fixed external forcing**

304 The standalone spin-up of ocean and land states is an efficient method to accelerate
305 the spin up process in the coupled model, especially in the PI control simulation. The



306 ocean component model is spun up with modern atmospheric and sea ice climatological
307 forcings, such as radiation, winds, precipitation, sea ice concentration and so on. The
308 offline integration length is 2000 (4000) model years for ocean component of NESM v3sr
309 (v3lr) model. The land surface initial condition is adopted from MPI-ESM-LR model
310 which has active dynamic vegetation and carbon cycle. The initial conditions of the
311 atmospheric and sea ice model in the coupled system used the modern observations. The
312 pre-industry control simulation is performed following the CMIP6 protocol with forcing
313 fixed at the year 1850 or around 1850s. The choice of time point or decadal mean forcing
314 is to minimize the initial shock of the ensuing historical simulation. The earth orbital
315 parameters, greenhouse gases, ozone concentration, land surface conditions are fixed at
316 their 1850 values. The solar constant used is the 11 years mean from 1850-1860. The
317 natural tropospheric aerosol and 1850s mean stratospheric aerosol forcing were employed
318 in the coupled system. During the whole PI simulation, there was no land use/land cover
319 change. The coupled model was spun up for 400 years so that the model reached an
320 equilibrium state. After that, a 500 years PI simulation is conducted and evaluated in this
321 study.

322 One of major purposes of the PI control experiment is to verify the model's stability in
323 the perpetual, unchanged forcing conditions. In this section, emphasis will put on
324 evaluation of the equilibrium state of the top-of-atmosphere (TOA), atmosphere-ocean-
325 sea ice interface to reveal the energy, water, and mass conservation of the whole system.
326 The energy input at the TOA is the major energy source for the Earth System. It is vital to
327 minimize the net energy imbalance at the TOA and surface, which can avoid temperature
328 drift in the system. The major indicators are the land surface temperature and ocean



329 surface temperature; they also work as the direct monitor of system energy conservation.
330 The precipitation is the most important part of global hydrological cycle, which involves
331 the energy exchange, as well as mass exchange among each climate system components.
332 The ocean salinity is sensitive to the state of surface hydrological cycle, land runoff and
333 sea ice melting/formation process. Sea ice extent is a good indicator of sea ice amount in
334 both Arctic and Antarctic regions, and it is sensitive to ocean heat content drift and high
335 latitude energy transfer. To better quantify the climate drifts, linear trends were calculated
336 for all evaluation variables.

337 The time evolution of global mean energy budget at the TOA, Earth surface and ocean
338 surface are shown in Fig. 2. The global mean net shortwave radiation at the TOA
339 averaged over the 500-year integration is 238.55Wm^{-2} and the corresponding outgoing
340 longwave radiation (OLR) is 238.39Wm^{-2} , resulting in a net atmospheric energy gain of
341 0.17Wm^{-2} . The net heat budget at the TOA shows a negligible decreasing trend of -
342 $0.0041\text{Wm}^{-2}(100\text{yr})^{-1}$. At the Earth surface, the net energy imbalance is 0.31Wm^{-2} in the
343 whole integration period with an insignificant decreasing trend of $-0.00576\text{Wm}^{-2}(100\text{yr})^{-1}$.
344 The negative trends are shown at both the TOA and surface, indicating the coupled
345 system could lead to a more stable state when the integration extends. Note that there is a
346 difference of 0.14Wm^{-2} between surface and TOA net energy budget, which means the
347 model atmosphere gains artificial energy. This problem is found also in the AMIP
348 experiment.

349 The trends in the surface temperature indices, namely global mean surface air
350 temperature, land surface temperature and SST, reveal the energy conservation and
351 stability as well as the stability of air-sea-sea ice interaction in the coupled system (Fig.



352 3). The mean value of the near surface air temperature (TAS) is 14.2 °C in the entire
353 period, and the linear trend of TAS is $-0.0021 \text{ °C (100yr)}^{-1}$. This trend is mainly attributed
354 to the land surface temperature rather than SST. The linear trend of land surface
355 temperature is $-0.016 \text{ °C (100yr)}^{-1}$. The slow balance of terrestrial (land) vegetation may
356 be one of the reasons. The global time-mean SST is 17.7 °C, which is consistent with the
357 observation measured during the decade of 1850-1860. The negligible SST trend ($-$
358 $0.0073 \text{ °C (100yr)}^{-1}$) indicates the global mean SST reached a quasi-equilibrium state. As
359 the most important component of global hydrological cycle, the global mean precipitation
360 has nearly no trend (Fig. 3). It is of interest that the global mean SST exhibits a long-term
361 variability with a period of 50-100 years in this simulation. Possible mechanism and
362 processes causing this variability will be discussed in a follow-up study.

363 To further verify the stability of ocean component model, more variables are
364 represented in Fig. 4. At the beginning of the PI experiment (coupled model spin up), the
365 sea surface salinity (SSS) has a quick adjustment process. The global mean SSS is
366 decreased from 34.6 psu to 34.2 psu in 30 years. After the spin up, the mean value of SSS
367 is 34.2 psu, which is 0.5 psu fresher than the observed value. The long-term trend of SSS
368 is $-0.0077 \text{ psu (100yr)}^{-1}$, which indicates the ocean water flux is maintained at a relatively
369 stable state. Meanwhile, the global mean sea water salinity (SWS) is 34.7 psu with a
370 linear trend of $-0.0038 \text{ psu (100yr)}^{-1}$. The total sea water temperature has an increase
371 trend of $0.032 \text{ °C (100yr)}^{-1}$, this is consistent with the surface energy budget which shows
372 a 0.43 Wm^{-2} heating at the ocean surface. Furthermore, the linear trend at the last 100
373 year is smaller than the first 100 year. The decrease of linear trend implies the model
374 becomes more and more stable during the integration.



375 Atlantic Meridional Overturning Circulation (AMOC) is a major source of
376 decadal/multidecadal variability of Earth system, and influences the Arctic sea ice extent
377 variability over Atlantic sector (Mahajan et al. 2011). The time series of the maximum
378 strength of the Atlantic Meridional Overturning Circulation (AMOC) at 26.5°N is
379 evaluated. The mean strength of AMOC is 14.8 sv, which is close to the modern
380 observational value (Cunningham et al. 2007) . The AMOC strength has a small linear
381 trend and significant multidecadal variability.

382 The middle and high latitude climate, as well as AMOC, is largely affected by sea ice
383 state and its variability. Following the IPCC report, the February, September and annual
384 mean of Northern and Southern Hemisphere sea ice extents (SIEs) are diagnosed for the
385 entire PI experiment period. The time evolutions of SIEs are plotted in Fig. 5. In the
386 Northern Hemisphere (NH), the annual mean, February and September mean SIE are 11
387 $\times 10^6 \text{ km}^2$, $12.7 \times 10^6 \text{ km}^2$, and $7.58 \times 10^6 \text{ km}^2$, respectively. The trends of SIE over the
388 NH in the annual mean, February and September mean SIE are $0.039 \times 10^6 \text{ km}^2(100\text{yr})^{-1}$,
389 $0.06 \times 10^6 \text{ km}^2(100\text{yr})^{-1}$, and $0.02 \times 10^6 \text{ km}^2(100\text{yr})^{-1}$, respectively. These trends are small,
390 suggesting that the Arctic SIE maintains a steady state. Over the SH, on the other hand,
391 the trends in the annual mean, February and September mean SIE are $-0.07 \times 10^6 \text{ km}^2$
392 $(100\text{yr})^{-1}$, $-0.002 \times 10^6 \text{ km}^2 (100\text{yr})^{-1}$, and $-0.1 \times 10^6 \text{ km}^2(100\text{yr})^{-1}$, respectively. This
393 indicates that a significant trend exists in the SH September only. The annual mean,
394 February and September mean SIEs are $7.27 \times 10^6 \text{ km}^2$, $1.73 \times 10^6 \text{ km}^2$, and 11.7×10^6
395 km^2 , respectively, indicating the SIEs are even less than recent decade's observation (e.g.,
396 1980-2009). The bias of the SH sea ice extent is related to the extensive solar radiation
397 over the Southern Ocean although the model overestimated cloud cover over there. This



398 is in part due to the thinner cloud optical depth in the simulated low-level cloud and
399 shallow mixed layer depth over the Southern Ocean (Sterl et al. 2012).

400 **5. Simulated climatology**

401 The climatological mean states of some key fields for energy and water balance
402 obtained from the average results for the last 100 year of the PI control run are compared
403 with observations, including Outgoing Longwave Radiation (OLR), SST, precipitation,
404 and sea surface salinity. The observed OLR data covers the period of 2001-2014 and the
405 observed SST is averaged over the period of 1870-1880. The rest of mean states are
406 derived for the period of 1979-2008.

407 Figure 6 shows the outgoing longwave radiation (OLR) which is balanced by the TOA
408 net downward solar radiation and represents the atmospheric and cloud top temperature
409 distribution. The global mean OLR is 238.45 Wm^{-2} in the model that is close to the
410 counterpart from the CERES data and the differences are within the range of uncertainty
411 among different observations. The model simulates well the vigorous deep convection-
412 related low OLR over the Indo-Pacific warm pool as well as the high OLR in the desert
413 and subtropical regions. However, the model overestimates the OLR over the majority of
414 ITCZ, Indo-Pacific warm pool regions, and the off-South American coast region in the
415 South Pacific. The model also underestimates the OLR in the North Atlantic storm track
416 and western part of the Pacific subtropical high regions. These biases arise primarily from
417 the errors in simulated cloud fields.

418 Figure 7 represents the simulated SST and its bias. SST is one of the most important
419 variables in the coupled system which reflects the quality of the model's simulation of



420 atmosphere-ocean interaction processes. The model well captures global distribution of
421 SST with a warm pool in the Indo-Pacific region and the cold tongue over the eastern
422 Pacific. There are warmer biases in the Southern Ocean and off the western coasts of
423 America and Africa, which link to the excessive downward shortwave radiation induced
424 by the negative bias in simulated stratiform clouds. Significant cold SST biases are found
425 in the high-latitude North Atlantic around 50°N with a maximum negative bias of -4K.
426 Cold biases are also seen in the subtropical North Pacific and North Atlantic.

427 Figure 8 compares the spatial pattern of observed and simulated precipitation. The
428 simulated precipitation pattern and intensity resemble the observations (pattern
429 correlation coefficient, PCC=0.85), which capture the observed rain bands over ITCZ,
430 South Pacific Convergence Zone (SPCZ), tropical Indian Ocean and the midlatitude
431 storm track regions. However, the so-called double-ITCZ precipitation bias exists in the
432 Pacific Ocean and Atlantic Ocean, which is likely linked to the deficiency in deep
433 convective parameterization that results in insufficient stratocumulus clouds (Bacmeister
434 et al. 2006, Song and Zhang 2009). The precipitation bias shows a dipole pattern over the
435 tropical Indian Ocean. From an atmospheric point of view, such a model deficiency is
436 mainly attributed to the SST bias over the tropics, but it is essentially a coupled model
437 bias.

438 The sea surface salinity (SSS) is an integrated indicator for the hydrological
439 interaction among ocean, atmosphere, land runoff and sea ice, as well as ocean
440 circulation. Accurate simulation of ocean circulation in climate models is essential for
441 correct estimation of the transient ocean heat uptake and climate response, sea level rise,
442 and coupled modes of climate variability. Figure 10 shows the observed climatological



443 SSS and the model bias. In general, the model simulates realistically the high SSS over
444 the subtropics, where precipitation is low and evaporation is high, and the relatively low
445 SSS over the ITCZ region where precipitation is heavy. The global mean SSS has a
446 negative bias of 0.5psu, which is mainly due to the fresh bias over the North Atlantic and
447 the western equatorial Pacific. Over the western equatorial Pacific, extensive
448 precipitation is the major cause. Over the North Atlantic, the excessive net input of fresh
449 water is a primary cause, which is augmented by weak evaporation at high latitudes. The
450 fresh water bias in the North Atlantic can also be attributed to the bias in simulated North
451 Atlantic Currents and excessive sea ice melt over the Labrador Sea. Previous studies
452 pointed out that the fresh bias over high latitudes of North Atlantic can weaken ocean
453 convection, so that weaken the Atlantic Meridional Overturning Circulation (AMOC).

454 **6. Climate sensitivity to CO₂ forcing**

455 Quantification of climate response to different forcing and estimation of the associated
456 radiative forcing can be benefited from sensitive experiments with a single perturbation
457 forcing, such as an abruptly quadrupling CO₂ (abrupt-4xCO₂) simulation and a 1% yr⁻¹
458 CO₂ increase (1pctCO₂) experiments. Following the CMIP6 protocols, two CO₂
459 experiments are designed to document basic aspects of the NESM v3 model response to
460 greenhouse gas forcing. They are both branched from the PI simulation and the only
461 difference is the imposed CO₂ concentrations. In the abrupt-4xCO₂ experiment, the
462 atmospheric CO₂ concentration is abruptly quadrupled (1139 ppm) with respect to the PI
463 condition (274.75 ppm) in the very beginning of the experiment. The 1pctCO₂ is
464 designed as gradually increasing the CO₂ concentration at the rate of 1% per year. Both



465 experiments were initiated at the end of year 100 of the PI experiments, and each of them
466 was integrated for 150 yrs.

467 Figure 10 shows the global annual mean surface air temperature (TAS) changes with
468 respect to its mean value in the PI experiment. Once the atmospheric CO₂ instantaneous
469 quadrupling, the radiative forcing defined by the net downward heat flux induced by the
470 changing atmospheric carbon dioxide concentration forces the stratospheric and
471 tropospheric circulations to adjust, thereby changing the surface temperature. The TAS
472 rapidly increases by approximately 4.5K in the first 20 years in response to the imposed
473 radiative forcing. After the rapid initial increase, the TAS gradually increases, mitigating
474 the energy imbalance at the TOA.

475 The abrupt 4 xCO₂ experiment is used not only to diagnose the fast response of
476 the Earth system, but also to quantify the radiative forcing, as well as to estimate the
477 Equilibrium Climate Sensitivity (ECS). The ECS is regarded as the global equilibrium
478 TAS change in response to the quadrupling atmospheric carbon dioxide concentration. It
479 is also indicated by the product of the radiative forcing and the climate feedback
480 parameter. The regression of TOA energy imbalance and global mean TAS change is an
481 effective method to obtain those estimations (Gregory et al. 2004). It doesn't require the
482 equilibrium state of GCM. The intersection of regression line and the y-axis is recognized
483 as the adjusted radiative forcing, and the intersection on the x-axis is an indication of the
484 equilibrium temperature. The slope of the regression line is the climate feedback
485 parameter.



486 The relationship between the change in the net TOA energy imbalance and global
487 mean TAS change is plotted in Fig. 11. Figure 11 shows that the TOA radiative
488 imbalance is around 7.24 Wm^{-2} when the assumed global TAS is unchanged, although
489 the radiative forcing is affected by the rapid adjustments of stratosphere in the first year
490 and therefore reduced the effective radiative forcing (Gregory and Webb 2008). To
491 balance the net TOA energy, the regression predicted an equilibrium temperature change
492 of 7.38 K in this model, yields a climate feedback parameter of $-0.98 \text{ Wm}^{-2}\text{K}^{-1}$. Since the
493 radiative forcing is logarithmically related to the carbon dioxide concentration and the
494 climate feedback parameter is considered as a constant in a given model, even in the
495 presence of other forcing agents (Hansen et al. 2005), this gives the ECS of 3.69K .
496 Andrews et al. (2012) found that the CMIP5 ensemble mean of regressed $4\times\text{CO}_2$ adjusted
497 forcing is $6.89\pm 1.12 \text{ Wm}^{-2}$, and the climate feedback parameter is $-1.08\pm 0.29 \text{ Wm}^{-2}\text{K}^{-1}$,
498 with the ECS of $3.37\pm 0.29\text{K}$. The carbon dioxide-induced radiative forcing and climate
499 feedback parameter estimated by the NESM v3 model are comparable with CMIP5
500 model ensemble, albeit the estimated ECS is about 10% higher.

501 The climate sensitivity parameter consists of the longwave clear sky, shortwave clear
502 sky, longwave cloud forcing and shortwave cloud forcing terms. They are defined by the
503 heat flux differences between the abrupt- $4\times\text{CO}_2$ experiment and PI experiment. The sum
504 of the longwave cloud forcing and shortwave cloud forcing is the Cloud Radiative Effect
505 (CRE). Here the downward fluxes are defined as positive. Figure 12 shows the
506 relationship between the change in the global mean heat fluxes and the change in the
507 surface air temperature. The longwave clear sky slope is $-1.63 \text{ Wm}^{-2}\text{K}^{-1}$, which is partially
508 offset by the shortwave clear sky feedback ($0.68 \text{ Wm}^{-2}\text{K}^{-1}$), resulting in a residual



509 feedback strength of $-0.95\text{Wm}^{-2}\text{K}^{-1}$, which is close to the climate sensitivity parameter
510 estimated in this model ($-0.98\text{Wm}^{-2}\text{K}^{-1}$). The slopes of the shortwave and longwave cloud
511 forcing have nearly the same magnitude but with opposite signs, yielding a small positive
512 cloud radiative effect ($0.02\text{Wm}^{-2}\text{K}^{-1}$) in this model. The result here is consistent with the
513 conclusion derived from the analysis of the CMIP5 models, that is, a GCM with higher
514 sensitivity is associated with a positive CRE feedback. The CRE is a major contributor to
515 the uncertainty in climate sensitivity parameter in CMIP3 and CMIP5 models, although
516 its magnitude is small compared to other flux terms (Webb et al. 2006, Andrews et al.
517 2012).

518 Figure 13 displays the global distributions of temperature and precipitation in response
519 to the quadrupling CO_2 forcing, which are defined by the departure of the last 30-year
520 climatology from the corresponding climatology in the PI experiment. The most
521 pronounced warming is seen over the Arctic region where sea ice albedo feedback
522 dominates. The relative small temperature change is over the Southern Ocean and North
523 Atlantic. The warming is more significant over land than ocean, especially in the
524 Northern Hemisphere. The mean surface temperature over land and ocean are 8.0K and
525 5.2K, respectively. The equatorial Pacific shows an El Nino-like warming. The zonal
526 mean surface temperature change shows an obvious polar amplification, especially over
527 the Arctic Ocean; and stronger warming over the NH high latitudes and weak warming in
528 the SH middle latitudes. The Large NH temperature increase is attributed to the strong
529 warming over the Arctic Ocean and the large land area in the NH.

530 A direct consequence of global warming is the rising atmospheric specific humidity
531 and precipitation. The global mean precipitation is increased from 2.87mm day^{-1} to 3.12



532 mm day⁻¹, resulting in a precipitation increase of 1.4% per Kelvin global warming.
533 Significant precipitation increases are seen in the equatorial Pacific and Northern Indian
534 Ocean as well as along the Pacific storm track (Fig. 13). Decreased precipitation is
535 evident in the sub-tropical descent zones. Note that precipitation is decreased over the
536 Amazon region, where the model has a dry bias in climatology. The global distribution of
537 precipitation change appears to be dominated by the wet-get-wetter (Held and Soden,
538 2006) pattern.

539 In reality, the CO₂ increase is gradually rather than abrupt. The 1pctCO₂ experiment is
540 designed to examine the transient climate response (TCR), which is calculated by using
541 the global mean TAS change between the averaged 20-year period centered at the timing
542 of CO₂ doubling (year 60-80 in 1pctCO₂ experiment) and the PI experiment. The time
543 evolution of the global mean TAS anomalies with respect to the PI experiment is shown
544 in Fig 14. A linear increase of temperature anomalies is presented in the gradually CO₂
545 increasing experiment. The temperature anomalies averaged between year 60 and 80 are
546 2.16K. This value of TCR is significantly small than the ECS, demonstrating that the
547 ocean heat uptake delays surface warming. The estimation from CMIP5 models shows
548 that the mean TCR is 1.8±0.6K (Flato et al. 2013), implying that the NESM v3 is
549 comparable to other CGCMs.

550 **6. Conclusion**

551 The development of version 3 of the Nanjing University of Information Science and
552 Technology (NUIST) Earth System Model (NESM v3) aims at building up a
553 comprehensive numerical modeling laboratory for multi-disciplinary studies of the



554 Climate System and Earth System. As a subsequent version of NESM v1, it has upgraded
555 the atmospheric and land surface models, increased the ocean model resolution, improved
556 coupling conservation and modified model physics.

557 The NESM v3 couples the ECHAM v6.3 atmospheric model, JSBACH land surface
558 model, NEMO v3.4 ocean model, and CICE v4.1 sea ice model by using OASIS3-
559 MCT_3.0 coupler. The improvement of model physics mainly focuses on convective
560 parameterizations, cloud macrophysics and microphysics, and ocean-sea ice coupling.
561 The model physics modifications and parameters adjustments are targeted at (1)
562 obtaining stable long-term integrations and reasonable global mean states under the
563 preindustrial (PI) forcing, (2) mitigating the biases in the mean climatology and internal
564 modes of climate variability with respect to the modern observations in the present-day
565 forcing condition, and (3) simulating reasonable climate responses to transient and abrupt
566 CO₂ forcing.

567 A 500-yr PI experiment is conducted and analyzed to test the model's computational
568 stability. As shown in Sec. 4, the long-term climate drifts in NESM v3 are generally
569 negligibly small, especially in the global radiative energy and temperature. The simulated
570 net downward energy flux at the TOA and surface are 0.17 Wm⁻² and 0.35Wm⁻²,
571 respectively. The near-equilibrium model long-term temperature evolution is benefited
572 from the near-zero energy imbalance and negligibly small trends in the energy balance.
573 The global mean near surface air temperature is 14.2°C with a trend of -0.0096 °C
574 (100yr)⁻¹. The linear trends of the land surface and sea surface temperature are -0.016°C
575 (100yr)⁻¹ and -0.0026°C (100yr)⁻¹, respectively. However, the total sea water temperature
576 has a warming trend of 0.03°C (100yr)⁻¹, which can be explained by the small but



577 persistent positive downward energy flux into the ocean. The stable long-term evolutions
578 of precipitation, sea surface salinity (SSS) and sea water salinity (SWS) demonstrate the
579 conservation of global water. At the beginning of PI experiments spin up, there was a
580 freshening trend in SSS, which is associated with the ocean adjustment. The fresher SSS
581 has no significant influence on SWT. After the spin up, the global mean SSS and SWT
582 have no appreciable trends although the SSS is fresher than the observed counterpart. The
583 Northern Hemispheric annual mean, February, and September mean sea ice extent (SIE)
584 maintain a steady value at $11.4 \times 10^6 \text{ km}^2$, $13.4 \times 10^6 \text{ km}^2$, and $7.78 \times 10^6 \text{ km}^2$, respectively.
585 However, the simulated Southern Hemisphere SIE are less than present-day observation.
586 The conservation properties of NESM v3.0 are encouraging, fulfilling a highly desirable
587 constraint for climate models aiming for multidecadal, centennial and longer simulations.

588 The model simulates realistic OLR pattern, although it overestimates OLR over the
589 ITCZ and Indo-Pacific warm pool regions as well as off the South American coast in the
590 South Pacific whereas underestimates the OLR in the North Atlantic storm track and
591 western Pacific subtropical high regions. The annual mean SST is well produced in the
592 model, but large cold biases exist in the North Atlantic and significant warm biases in the
593 Southern Ocean. The biases in OLR and SST are primarily associated with the errors in
594 the simulated cloud fields except for the North Atlantic cold bias. The simulated mean
595 precipitation is reasonably realistic, but slightly suffers the double ITCZ syndrome. The
596 fresh bias in SSS in the tropical western North Pacific can be attributed to the extensive
597 precipitation and the fresh bias over the mid-latitude North Atlantic is related to
598 underestimated evaporation.



599 The model produces a radiative forcing, under the abrupt quadrupling carbon dioxide,
600 of 7.24 Wm^{-2} with a climate feedback parameter of $-0.98 \text{ Wm}^{-2} \text{ K}^{-1}$, yielding a warming of
601 7.38 K at the estimated equilibrium state. The transient climate sensitivity is 2.16 K
602 which is estimated from the $1\% \text{ yr}^{-1} \text{ CO}_2$ gradually increasing experiment. The NESM v3
603 model is amongst the more sensitive side of the CMIP5 class of global climate models.

604 The NESM v3 model's response to historical forcing, and the corresponding modern
605 climatology, internal and coupled modes of climate variability, as well as regional
606 climate variability will be discussed in detail in an accompanying paper later.

607

608 Code availability

609 Please contact Jian Cao (Email: jianc@nuist.edu.cn) to obtain the source code and data
610 of NESM v3.

611

612 **Acknowledgements**

613 This work is supported by the Nanjing University of Information Science and
614 Technology through funding the joint China-US Atmosphere-Ocean Research Center at
615 the University of Hawaii. Jian Cao is thankful for the support of National Key R&D
616 Program of China (2017YFA0603801). This is the IPRC publication number YYYY and
617 the ESMC publication number XXX.

618



619 **Reference**

- 620 Adcroft, A., Hill, C., Marshall, J.: Representation of topography by shaved cells in a
621 height coordinate ocean model. *Mon. Weather Rev.*, 125, 2293-2315, 1997.
- 622 Andrews, T., Gregory, J. M., Webb, M. J., Taylor, K. E.: Forcing, feedbacks and climate
623 sensitivity in CMIP5 coupled atmosphere-ocean climate models. *Geophysical*
624 *Research Letters*, 39(9), 2012.
- 625 Bacmeister, J. T., Suarez, M. J., and Robertson, F. R.: Rain reevaporation, boundary
626 layer–convection interactions, and Pacific rainfall patterns in an AGCM. *J. Atmos.*
627 *Sci.*, 63, 3383–3403, 2006.
- 628 Barnier, B., G. Madec, T. Penduff, J.-M. Molines, A.-M. Treguier, J. L. Sommer, A.
629 Beckmann, A. Biastoch, C. Boning, J. Dengg, C. Derval, E. Durand, S. Gulev, E.
630 Remy, C. Talandier, S. Theetten, M. Maltrud, J. McClean, and Cuevas B. D.:
631 Impact of partial steps and momentum advection schemes in a global ocean
632 circulation model at eddy-permitting resolution. *Ocean Dyn.*, 56, 543–567. 2006.
- 633 Bernard, B., Madec, G., Penduff, T., et al: Impact of partial steps and momentum
634 advection schemes in a global ocean circulation model at eddy-permitting
635 resolution. *Ocean Dyn.*, 56, 543-567, 2006.
- 636 Brovkin, V., Boysen, L., Raddatz, T., Gayler, V., Loew, A., and Claussen, M.: Evaluation
637 of vegetation cover and landsurface albedo in MPI-ESM CMIP5 simulations, *J.*
638 *Adv. Model. Earth Syst.*, 5, 48–57, doi:10.1029/2012MS000169, 2013.
- 639 Cao, J., and Wu, L.: Asymmetric impact of last glacial maximum ice sheets on global
640 monsoon activity. *Journal of the Meteorological Sciences*, 36(4):425-435, 2016.



- 641 Cao, J., Wang, B., Xiang, B., Li, J., Wu, T., Fu, X., Wu, L. Min, J.: Major modes of
642 short-term climate variability in the newly developed NUIST Earth System Model
643 (NESM). *Adv. Atmos. Sci.*, 32(5), 585–600, doi: 10.1007/s00376-014-4200-6,
644 2015.
- 645 Cunningham, S. A., Kanzow, T., Rayner, D., Baringer, M. O., Johns, W. E., Marotzke, J.,
646 Longworth, H. R., Grant, E. M., Hirschi, J. J.-M., Beal, L. M., Meinen, C.S.,
647 Bryden, H. L.: Temporal variability of the Atlantic Meridional Overturning
648 Circulation at 26°N. *Science*, 317, 935-938, 2006.
- 649 Eyring, V., Bony, S., Meehl, G. A., Senior, C. A., Stevens, B., Stouffer, R. J., and Taylor,
650 K. E.: Overview of the Coupled Model Intercomparison Project Phase 6 (CMIP6)
651 experimental design and organization, *Geosci. Model Dev.*, 9, 1937-1958,
652 doi:10.5194/gmd-9-1937-2016, 2016.
- 653 Flato, G., Marotzke, J., Abiodun, B., Braconnot, P., Chou, S. C., Collins, W., Cox, P.,
654 Driouech, F., Emori, S., Eyring, V., Forest, C., Gleckler, P., Guilyardi, E., Jakob,
655 C., Kattsov, V., Reason, C., and Rummukainen, M.: Evaluation of Climate Models,
656 in: *Climate Change 2013: The Physical Science Basis, Contribution of Working*
657 *Group I to the Fifth Assessment Report of the Intergovernmental Panel on Climate*
658 *Change*, edited by: Stocker, T. F., Qin, D., Plattner, G.-K., Tignor, M., Allen, S. K.,
659 Boschung, J., Nauels, A., Xia, Y., Bex, V., and Midgley, P. M., Cambridge
660 University Press, Cambridge, United Kingdom and New York, NY,USA, 2013.
- 661 Fu, X., and Wang, B.: Critical roles of the stratiform rainfall in sustaining the Madden-
662 Julian Oscillation: GCM Experiments. *J. Climate*, 22 (14) 3939–3959, 2009.



- 663 Gent, P. R. and McWilliams, J. C.: Isopycnal mixing in ocean circulation models. *J. Phys.*
664 *Oceanogr.*, 20, 150-155, 1990.
- 665 Giorgetta, M. A., Roeckner, E. Mauritsen, T., Bader, J., Crueger, T., Esch, M., Rast, S.,
666 Kornbluh, L., Schmidt, H., Kinne, S. Hohenegger, C. Möbis, B. Krismer, T.,
667 Wieners, K.–H. Stevens, B.: The Atmospheric General Circulation Model
668 ECHAM6: Model Description, Tech. rep., Max Planck Institute for Meteorology,
669 Hamburg, Germany. 2013.
- 670 Gregory, J. M., and Webb, M. J.: Tropospheric adjustment induces a cloud component in
671 CO₂ forcing, *J. Clim.*, 21, 58–71, doi:10.1175/2007JCLI1834.1, 2008.
- 672 Gregory, J. M., Ingram, W. J., Palmer, M. A., Jones, G. S. Stott, P. A. Thorpe, R. B.
673 Lowe, J. A., Johns, T. C., and Williams, K. D.,: A new method for diagnosing
674 radiative forcing and climate sensitivity, *Geophys. Res. Lett.*, 31, L03205,
675 doi:10.1029/2003GL018747, 2004.
- 676 Ham, Y.-G., Kug, J.-S.: ENSO phase-locking to the boreal winter in CMIP3 and CMIP5
677 models. *Clim Dyn* 43:305–318.doi:10.1007/s00382-014-2064-1,2014.
- 678 Hansen, J., et al. Efficacy of climate forcings, *J. Geophys. Res.*, 110, D18104,
679 doi:10.1029/2005JD005776, 2005.
- 680 Hansen, J., Nazarenko, L., Ruedy, R., Sato, M., Willis, J., DelGenio, A., Koch, D., Lacis,
681 A., Lo, K., Menon, S., Novakov, T., Perlwitz, J., Russell, G., Schmidt, G.A.,
682 and Tausnev, N.: Earth's energy imbalance: Confirmation and
683 implications. *Science*, 308, 1431-1435, doi:10.1126/science.1110252, 2005.
- 705 Held, I. M., and Soden, B. J.: Robust response of the hydrological cycle to global
706 warming, *J. Clim.*, 19, 5686 – 5699, 2006.



- 707 Hourdin, F., Mauritsen, T., Gettelman, A., Golaz, J.-C., Balaji, V., Duan, Q., Folini, D., Ji,
708 D., Klocke, D., Qian, Y., Rauser, F., Rio, C., Tomassini, L., Watanabe, M., and
709 Williamson, D.: The art and science of climate model tuning. *Bulletin of the*
710 *American Meteorological Society* 98, 589–602, doi:10.1175/bams-d-15-00135.1,
711 2017.
- 712 Hunke, E. C.: Thickness sensitivities in the CICE sea ice model. *Ocean Modelling*, 34, pp.
713 137-149. doi:10.1016/j.ocemod.2010.05.004. LA-UR-10-00585, 2010.
- 714 Hunke, E. C., and Lipscomb, W. H.: CICE: The Los Alamos Sea Ice Model
715 Documentation and Software User's Manual Version 4.1. LA-CC-06-012, T-3
716 Fluid Dynamics Group, Los Alamos National Laboratory, Los Alamos N.M, 2010.
- 717 Iacono, M. et al.: Radiative forcing by long-lived greenhouse gases: Calculations with the
718 AER radiative transfer models. *J. Geophys. Res.*, 113, 2008.
- 719 Lee, J. Y., and Wang, B.: Future change of global monsoon in the CMIP5. *Climate*
720 *Dynamics*, 42, 101-119, 2014.
- 721 Lengaigne, M., Madec, G. Bopp, L. Menkes, C. Aumont, O. and Cadule, P.: Bio-physical
722 feedbacks in the Arctic Ocean using an Earth system model. *Geophys. Res. Lett.*,
723 36, L21602. doi: 10.1029/2009GL040145, 2009.
- 724 Li, J., Wang, B., and Yang, Y.M.: Retrospective seasonal prediction of summer monsoon
725 rainfall over West Central and Peninsular India in the past 142 years. *Climate Dyn.*,
726 48(7), 2581-2596, 2017.
- 727 Locarnini, R. A., Mishonov, A. V., Antonov, J. I., Boyer, T. P., Garcia, H. E., Baranova,
728 O. K., Zweng, M. M., and Johnson, D. R. *World Ocean Atlas 2009, Volume 1:*
729 *Temperature*. S. Levitus, Ed. NOAA Atlas NESDIS 68, U.S. Government Printing



- 730 Office, Washington, D.C., 184 pp, 2010.
- 731 Loeb, N. G., Wielicki, B. A., Doelling, D. R., Smith, G. L., Keyes, D. F.; Kato, S.,
732 Manalo-Smith, N., Wong, T.: Toward Optimal Closure of the Earth's Top-of-
733 Atmosphere Radiation Budget *Journal of Climate*, 22(3), 748-766.
734 <http://dx.doi.org/10.1175/2008JCLI2637.1>, 2009.
- 735 Lott, F.: Alleviation of Stationary Biases in a GCM through a Mountain Drag
736 Parameterization Scheme and a Simple Representation of Mountain Lift Forces.
737 *Mon Weather Rev*, 127 (5), 788-801, 1999.
- 738 Lumpkin, R., and Speer, K.: Global ocean meridional overturning. *J. Phys. Oceanogr.*, 37,
739 2550–2562, 2007.
- 740 Madec, G. and Imbard M. : A global ocean mesh to overcome the North Pole singularity.
741 *Climate Dynamics*, 12, 381-388,1996.
- 742 Mahajan., S., Zhang, R., Delworth, T. L.: Impact of the Atlantic Meridional Overturning
743 circulation (AMOC) on Arctic surface air temperature and sea ice variability.
744 *Journal of Climate*, 24, 6573-81, 2011.
- 745 Meehl, G. A., Boer, G.J., Covey, C. Latif, M. and Stouffer, R. J.: The Coupled Model
746 Intercomparison Project (CMIP). *Bull. Amer. Metero. Soc.*, 81, 313-318, 2000.
- 747 Miller, M. J., T. N. Palmer, and R. Swinbank: Parametrization and influence of
748 subgridscale orography in general circulation and numerical weather prediction
749 models. *Meteorl. Atmos. Phys.*, 40 (1), 84-109, 1989.
- 750 Nordeng, T. E.: Extended versions of the convective parameterization scheme at
751 ECMWF and their impact on the mean and transient activity of the model in the
752 tropics. Tech. Rep. 206, ECMWF, Reading, 1994.



- 753 Raddatz, T. J., Reick, C.H., Knorr, W., Kattge, J., Roeckner, E., Schnur, R., Schnitzler,
754 K.-G., Wetzell, P., Jungclaus, J.: Will the tropical land biosphere dominate the
755 climate-carbon cycle feedback during the twenty-first century? *Clim. Dyn.*, 29,
756 565–574, 2007.
- 757 Rayner, N. A., Parker, D. E., Horton, E. B., Folland, C. K., Alexander, L. V., Rowell, D.
758 P., Kent, E. C., and Kaplan, A.: Global analyses of sea surface temperature, sea ice,
759 and nightmarine air temperature since the late nineteenth century. *J. Geophys. Res.*,
760 108, 4407, doi:10.1029/2002JD002670, 2003.
- 761 Redi, M. H.: Oceanic isopycnal mixing by coordinate rotation, *J. Phys. Oceanogr.*, 12,
762 1154-1158, 1982.
- 763 Rothrock, D. A.: The energetics of the plastic deformation of pack ice by ridging. *J.*
764 *Geophys. Res.*, 80, 4514–4519, 1975.
- 765 Roulet, G. and Madec, G.: Salt conservation, free surface and varying volume: A new
766 formulation for ocean GCMs. *J. Geophys. Res.*, 105, 23927-23942, 2000.
- 767 Schmidt, G. A., Bader, D., Donner, L. J., Elsaesser, G.S., Golza, J.-C., Hannay, C.,
768 Molod, A., Neale, R., Saha, S.: Practice and philosophy of climate model tuning
769 across six U.S. modeling centers. *Geosci. Model Dev. Discuss.*, doi:10.5194/gmd-
770 2017-30, 2017.
- 771 Simmons, A. J. and Burridge, D. M.: An energy and angular-momentum conserving
772 vertical finite difference scheme and hybrid vertical coordinates. *Mon. Wea. Rev.*,
773 109,758–766, 1981.



- 774 Song, X., and Zhang, G.: Convection parameterization, tropical Pacific double ITCZ, and
775 upper-ocean biases in the NCAR CCSM3. Part I: Climatology and atmospheric
776 feedback. *J. Climate*, 22, 4299–4315, 2009.
- 777 Sterl., A., Bintanja, R., Brodean, L., Gleeson, E., Koenigk, T., Schmith, T., Semmler, T.,
778 Severijns, C., Wyser, K., Yang, S.: A look at the ocean in the EC-Earth climate
779 model. *Climate Dynamics* 29:2631-2657, 2012.
- 780 Stevens, B., et al., 2012: The atmospheric component of the MPI-M Earth System Model:
781 ECHAM6. *J. Adv. Model. Earth Syst.*, doi:10.1002/jame.20015.
- 782 Tiedtke, M.: A Comprehensive Mass Flux Scheme for Cumulus Parameterization in
783 Large-Scale Models. *Mon Weather Rev*, 117 (8), 1779-1800, 1989.
- 784 Urrego-Blanco, J. R., N. M. Urban, E. C. Hunke, A. K. Turner, and N. Jeffery,
785 Uncertainty quantification and global sensitivity analysis of the Los Alamos sea ice
786 model, *J. Geophys. Res. Oceans*, 121, 2709–2732, doi:10.1002/2015JC011558,
787 2016.
- 788 Valcke, S., and Coquart, L.: OASIS3-MCT User Guide, OASIS3-MCT 3.0. CERFACS
789 Technical Report, CERFACS TR/CMGC/15/38, Toulouse, France., available at:
790 http://www.cerfacs.fr/oa4web/oasis3mct_3.0/oasis3mct_UserGuide.pdf, 2015.
- 791 Wengel, C., Latif, M., Park, W., Harlaß, J., Bayr, T.: Seasonal ENSO phase locking in the
792 Kiel Climate Model: The importance of the equatorial cold sea surface temperature
793 bias. *Clim Dyn.* DOI 10.1007/s00382-017-3648-3, 2017.
- 794 Xie, P., and Arkin, P.A.: Global precipitation: A 17-year monthly analysis based on
795 gauge observations, satellite estimates, and numerical model outputs. *Bull. Amer.*
796 *Meteor. Soc.*, 78, 2539 – 2558, 1997.



797 Zalesak, S. T.: Fully multidimensional flux corrected transport algorithms for fluids. J.
798 Comput. Phys., 31, 335–362, 1979.
799
800
801
802
803
804
805
806
807
808
809
810
811
812
813
814
815
816
817
818
819



820 List of Figure:

821 Fig.1. Coupled structure of NESM v3 model.

822 Fig. 2. Radiative energy balances in NESM v3. (a) Time series of the net radiative energy fluxes
823 at TOA (downward, Wm^{-2}) and (b) the net heat flux at the Earth surface (Wm^{-2} bottom) from year
824 0 to year 500 in the Preindustrial control experiment. The long-term mean value and trend are
825 indicated in the left upper corner. The black lines indicate annual mean values and the red lines
826 indicate their 9-yr running mean values.

827 Fig. 3. Results from the Preindustrial control experiment. Annual mean time series of the surface
828 temperature and precipitation from year 0 to year 500 in the Preindustrial control experiment,
829 from top, near surface air temperature ($^{\circ}\text{C}$), land surface temperature ($^{\circ}\text{C}$), sea surface
830 temperature ($^{\circ}\text{C}$), and precipitation (mmd^{-1}). The long-term mean value and trend are indicated in
831 the left upper corners. The black lines are annual mean values and the red lines are their 9-yr
832 running mean values.

833 Fig. 4. Results from the Preindustrial control experiment. Annual mean time series of the ocean
834 variables from year 0 to year 500 from top, sea surface salinity (psu); sea water salinity (psu); sea
835 water temperature ($^{\circ}\text{C}$), AMOC strength at 26.5° N (sv). The long-term mean value and trend
836 are indicated in the left upper corner. The black lines are annual mean values and the red lines are
837 their 9-yr running mean values.

838 Fig. 5. Results from the Preindustrial control experiment. The Northern Hemisphere (NH) and
839 Southern Hemisphere (SH) sea ice extents (SIEs, unit: 10^6km^2) time series year 0 to year 500 in
840 the Preindustrial control experiment. The black, blue and green lines represent the annual mean,
841 March and September SIEs, and the red lines are the corresponding 9-yr running mean. The long-
842 term trends of annual mean SIEs are indicated in the left upper corner of each panel.



843 Fig. 6. Annual mean outgoing longwave radiation (OLR in units of W m^{-2}) derived from
844 observation (top), the model simulation in the PI experiment (middle) and the model bias
845 (bottom). The observed OLR filed was derived from the Clouds and the Earth's Radiant Energy
846 System (CERES) dataset (Loeb et al. 2009).

847 Fig. 7. The same as in Fig. 6 but for annual mean of SST ($^{\circ}\text{C}$). The observed SST climatology
848 was derived from the Hadley Center sea-Ice and Sea Surface Temperature (HadISST, Rayner et
849 al., 2003) for the period of 1870-1880.

850 Fig. 8. The same as in Fig. 6 except for annual mean of precipitation (mm day^{-1}). The observed
851 precipitation was derived from a Merged precipitation dataset (Lee and Wang 2014), which is the
852 arithmetic mean of the monthly data from the Global Precipitation Climatology Project (GPCP)
853 version 2.2 (Adler et al., 2003) and Climate Prediction Center Merged Analysis of Precipitation
854 (CMAP, Xie and Arkin, 1997).

855 Fig. 9. Same as in Fig. 6 except for the annual mean sea surface salinity (psu). The observed SSS
856 data are from the World Ocean Atlas 2009 (WOA09) (Locarnini et al. 2010).

857 Fig. 10. Results from the abrupt quadrupling CO_2 experiment. Global-mean surface air
858 temperature change relative to the counterpart in the PI experiment. The red and black lines
859 indicate the results obtained from the NESMv3 and 10 CMIP5 models' MME, respectively.

860 Fig. 11. Results from the abrupt quadrupling CO_2 experiment. The relationships between the
861 change in the net TOA radiative flux and the global-mean surface air temperature in NESM v3
862 model. The solid line represents linear least squares regression fit to the 150 years of model
863 output data. The interception at $\delta T = 0$ indicates the adjusted radiative forcing ($F=7.24\text{Wm}^{-2}$). The
864 slope of the regression line measures the strength of the feedbacks in the climate system, the
865 climate feedback parameter ($-0.981\text{Wm}^{-2}\text{K}^{-1}$). The interception at x-axis gives the equilibrium δT
866 (7.38 K).



867 Fig. 12. Results from the abrupt quadrupling CO₂ experiment. The relationship between the
868 change in the global mean radiative fluxes and global mean surface air temperature change. The
869 climate feedback parameters (Wm⁻²K⁻¹) for the TOA longwave clear sky (red), shortwave clear
870 sky(green), longwave cloud forcing (blue), shortwave cloud forcing (light blue) and net cloud
871 radiative effect (black) are -1.63, 0.675, 0.31, -0.30, 0.02 Wm⁻²K⁻¹, respectively.

872 Fig. 13. Changes in the surface temperature (top) and precipitation (bottom) derived from the last
873 30-year climatology in the 150-year abrupt 4 x CO₂ experiments. The changes are with reference
874 to the corresponding climatological mean fields from the PI experiment. The right panels show
875 the corresponding zonal mean changes.

876 Fig. 14. Results from the 1%per year CO₂ increases experiment. Global mean annual surface air
877 temperature change relative to counterpart in the PI experiment. The red and black lines indicate
878 the results obtained from the NESMv3 and 10 CMIP5 models' MME, respectively. The average
879 temperature anomalies between year 60-80 is defined as transit climate sensitivity, which is
880 2.16K in the NESM v3 model.

881

882

883

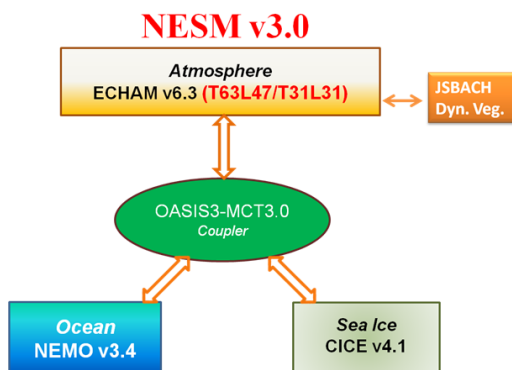
884

885

886

887

888



889

890

891 Figure1. Coupled structure of NESM v3 model.

892

893

894

895

896

897

898

899

900

901

902

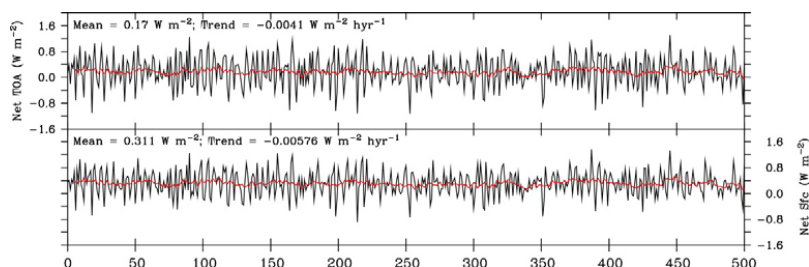
903

904

905

906

907



908

909 Figure 2 Radiative energy balances in NESM v3. (a) Time series of the net radiative energy
910 fluxes at TOA (downward, Wm^{-2}) and (b) the net heat flux at the Earth surface (Wm^{-2} bottom)
911 from year 0 to year 500 in the Preindustrial control experiment. The long-term mean value and
912 trend are indicated in the left upper corner. The black lines indicate annual mean values and the
913 red lines indicate their 9-yr running mean values.

914

915

916

917

918

919

920

921

922

923

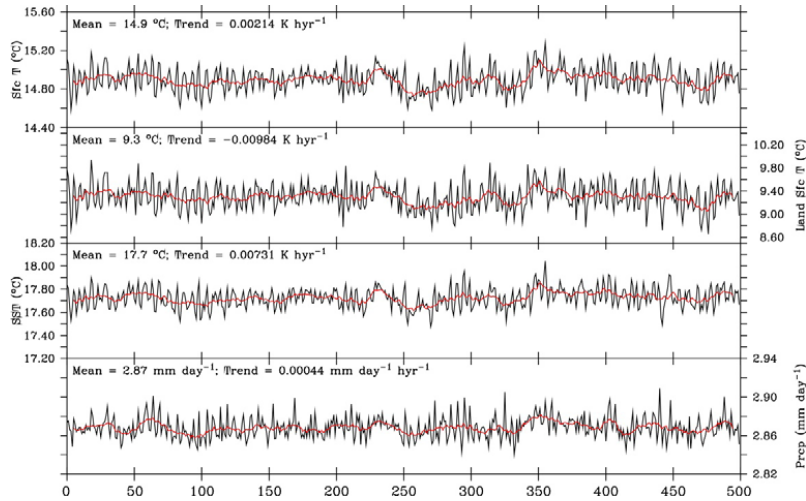
924

925

926

927

928



929

930 Figure 3 Results from the Preindustrial control experiment. Annual mean time series of the
931 surface temperature and precipitation from year 0 to year 500 in the Preindustrial control
932 experiment, from top, near surface air temperature (°C), land surface temperature (°C), sea
933 surface temperature (°C), and precipitation (mm day^{-1}). The long-term mean value and trend are
934 indicated in the left upper corners. The black lines are annual mean values and the red lines are
935 their 9-yr running mean values.

936

937

938

939

940

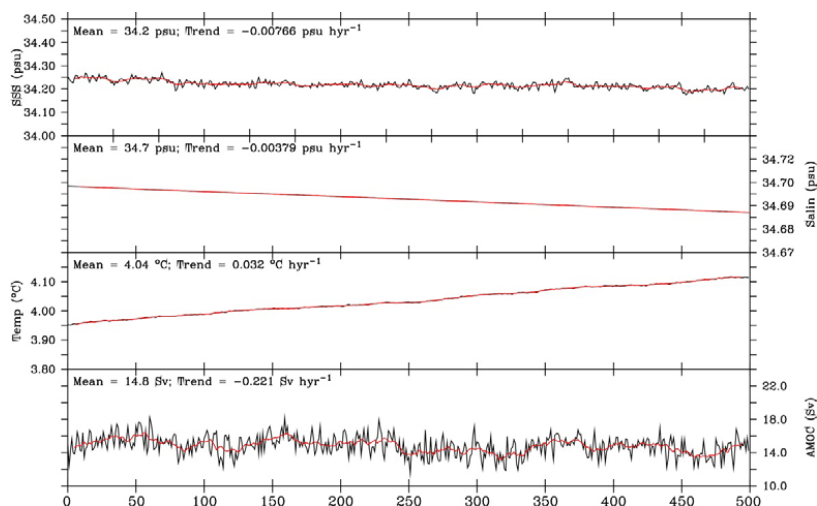
941

942

943

944

945



946

947 Figure 4 Results from the Preindustrial control experiment. Annual mean time series of the ocean
 948 variables from year 0 to year 500 from top, sea surface salinity (psu); sea water salinity (psu); sea
 949 water temperature (°C), AMOC strength at 26.5° N (sv). The long-term mean value and trend
 950 are indicated in the left upper corner. The black lines are annual mean values and the red lines are
 951 their 9-yr running mean values.

952

953

954

955

956

957

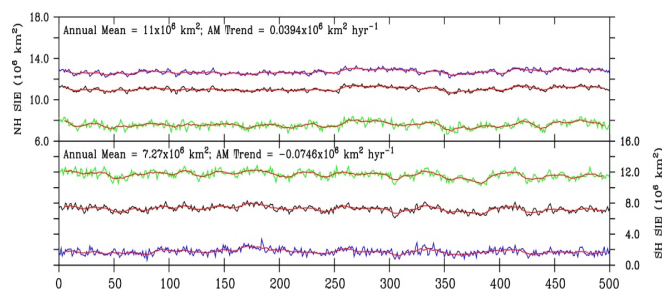
958

959

960

961

962



963

964 Figure 5 Results from the Preindustrial control experiment. The Northern Hemisphere (NH) and
 965 Southern Hemisphere (SH) sea ice extents (SIEs, unit: 10^6 km^2) time series year 0 to year 500 in
 966 the Preindustrial control experiment. The black, blue and green lines represent the annual mean,
 967 March and September SIEs, and the red lines are the corresponding 9-yr running mean. The long-
 968 term trends of annual mean SIEs are indicated in the left upper corner of each panel.

969

970

971

972

973

974

975

976

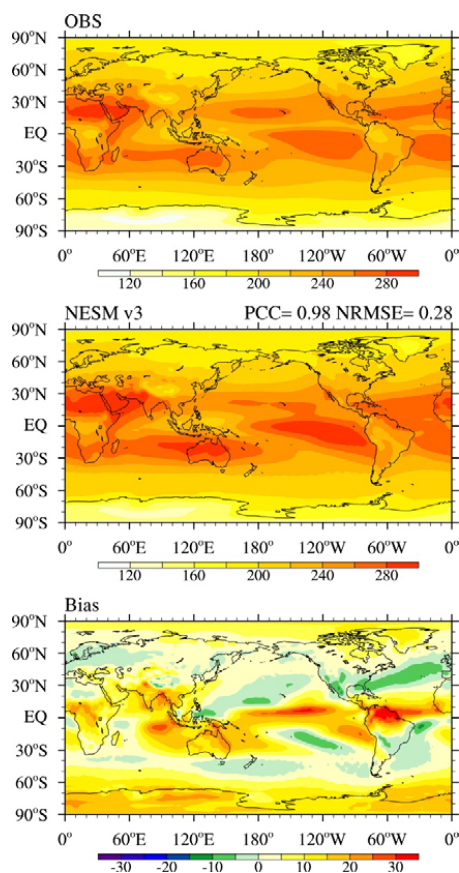
977

978

979

980

981



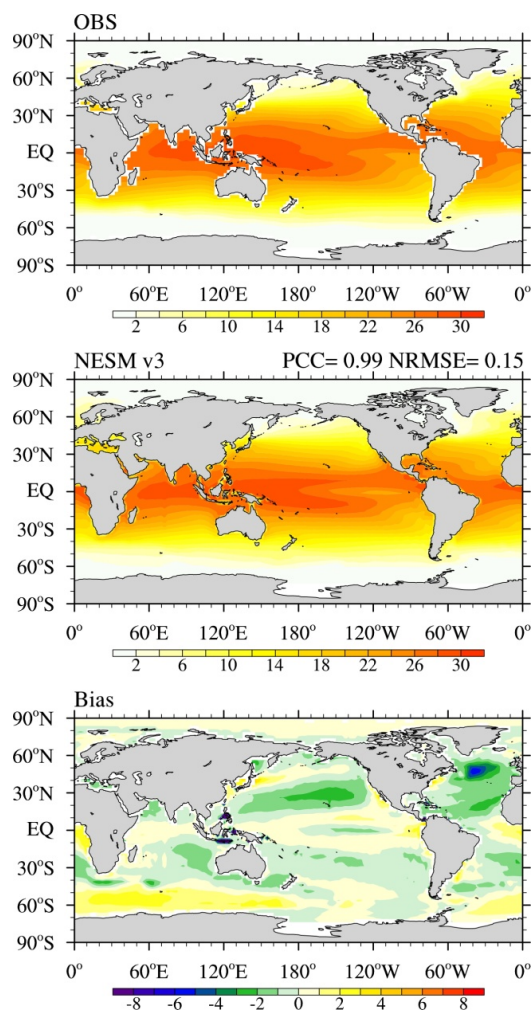
982

983 Figure 6 Annual mean outgoing longwave radiation (OLR in units of W m^{-2}) derived from
984 observation (top), the model simulation in the PI experiment (middle) and the model bias
985 (bottom). The observed OLR filed was derived from the Clouds and the Earth's Radiant Energy
986 System (CERES) dataset (Loeb et al. 2009).

987

988

989



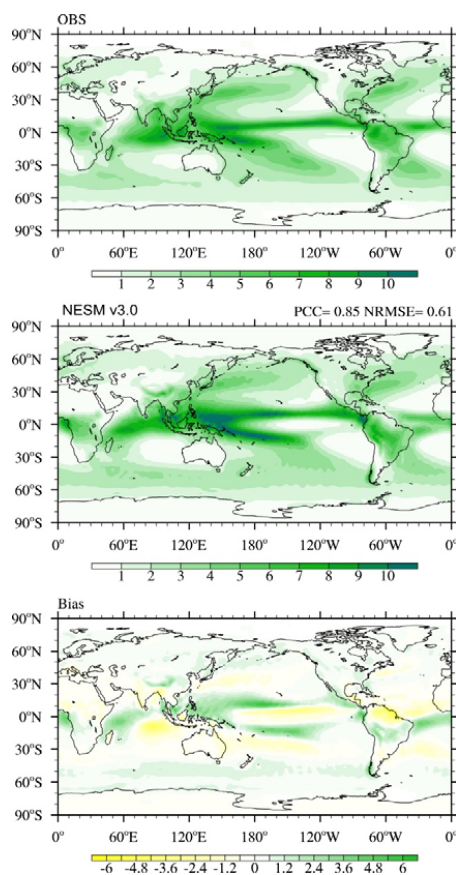
990

991 Figure 7 The same as in Fig. 6 but for annual mean of SST (°C). The observed SST climatology

992 was derived from the Hadley Center sea-Ice and Sea Surface Temperature (HadISST, Rayner et

993 al., 2003) for the period of 1870-1880.

994



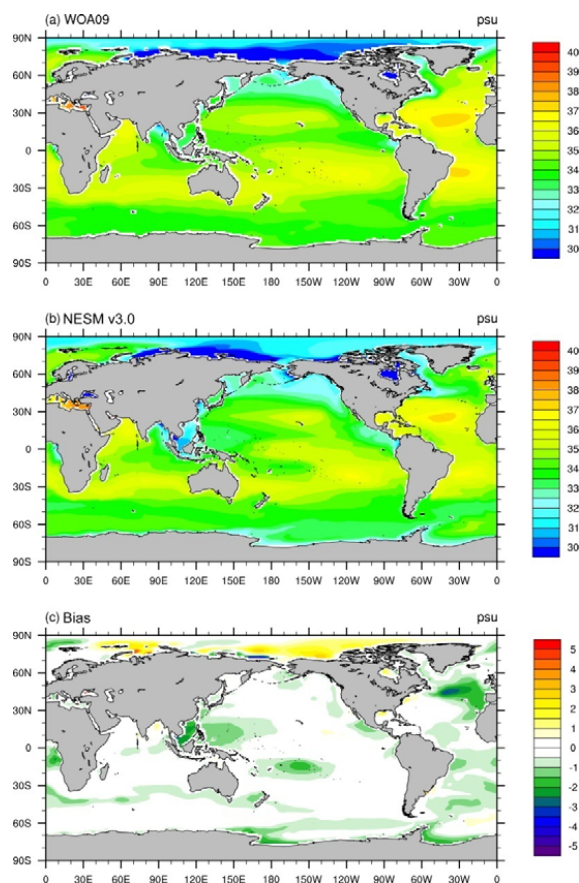
995

996 Figure 8 The same as in Fig. 6 except for annual mean of precipitation (mm day^{-1}). The observed
997 precipitation was derived from a Merged precipitation dataset (Lee and Wang 2014), which is the
998 arithmetic mean of the monthly data from the Global Precipitation Climatology Project (GPCP)
999 version 2.2 (Adler et al., 2003) and Climate Prediction Center Merged Analysis of Precipitation
1000 (CMAP, Xie and Arkin, 1997).

1001

1002

1003



1004

1005 Figure 9 Same as in Fig. 6 except for the annual mean sea surface salinity (psu). The observed

1006 SSS data are from the World Ocean Atlas 2009 (WOA09) (Locarnini et al. 2010).

1007

1008

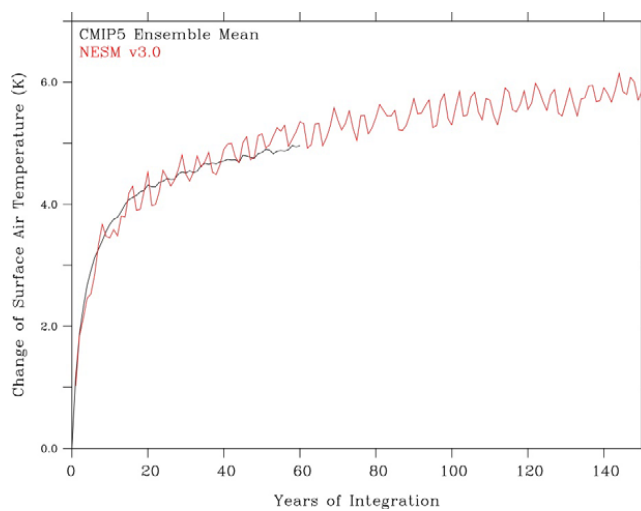
1009

1010

1011

1012

1013



1014

1015 Figure 10 Results from the abrupt quadrupling CO₂ experiment. Global-mean surface air
1016 temperature change relative to the counterpart in the PI experiment. The red and black lines
1017 indicate the results obtained from the NESMv3 and 10 CMIP5 models' MME, respectively.

1018

1019

1020

1021

1022

1023

1024

1025

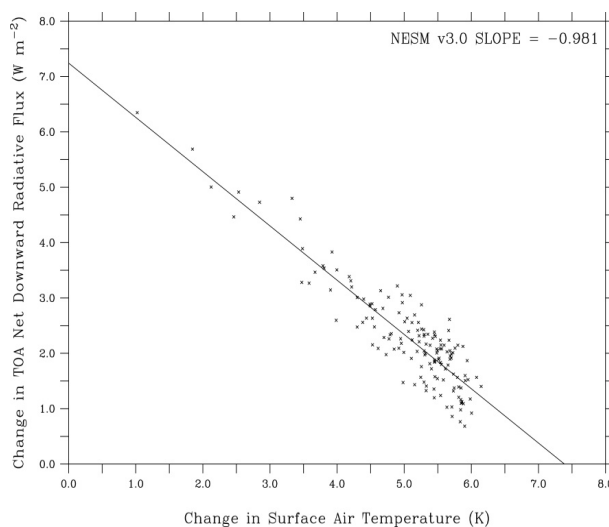
1026

1027

1028

1029

1030



1031

1032 Figure 11 Results from the abrupt quadrupling CO₂ experiment. The relationships between the
 1033 change in the net TOA radiative flux and the global-mean surface air temperature in NESM v3
 1034 model. The solid line represents linear least squares regression fit to the 150 years of model
 1035 output data. The interception at $\delta T = 0$ indicates the adjusted radiative forcing ($F=7.24\text{Wm}^{-2}$). The
 1036 slope of the regression line measures the strength of the feedbacks in the climate system, the
 1037 climate feedback parameter ($-0.981\text{Wm}^{-2}\text{K}^{-1}$). The interception at x-axis gives the equilibrium δT
 1038 (7.38 K).

1039

1040

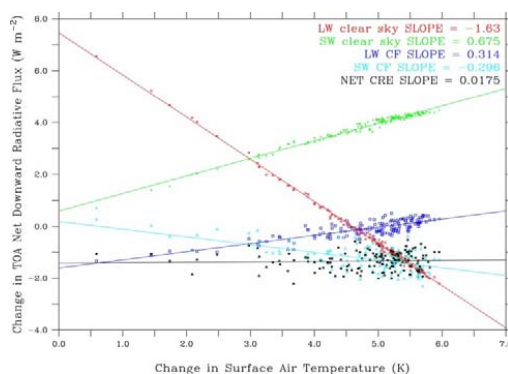
1041

1042

1043

1044

1045



1046

1047 Figure 12 Results from the abrupt quadrupling CO₂ experiment. The relationship between the
 1048 change in the global mean radiative fluxes and global mean surface air temperature change. The
 1049 climate feedback parameters (Wm⁻²K⁻¹) for the TOA longwave clear sky (red), shortwave clear
 1050 sky(green), longwave cloud forcing (blue), shortwave cloud forcing (light blue) and net cloud
 1051 radiative effect (black) are -1.63, 0.675, 0.31, -0.30, 0.02 Wm⁻²K⁻¹, respectively.

1052

1053

1054

1055

1056

1057

1058

1059

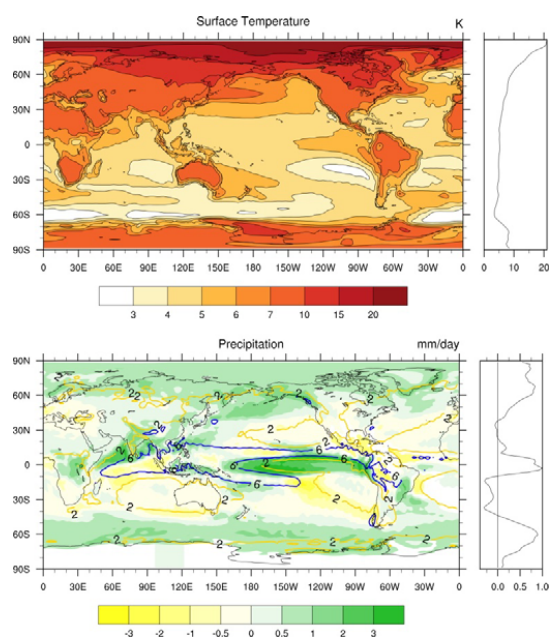
1060

1061

1062

1063

1064



1065

1066 Figure 13 Changes in the surface temperature (top) and precipitation (bottom) derived from the
1067 last 30-year climatology in the 150-year abrupt $4 \times \text{CO}_2$ experiments. The changes are with
1068 reference to the corresponding climatological mean fields from the PI experiment. The right
1069 panels show the corresponding zonal mean changes.

1070

1071

1072

1073

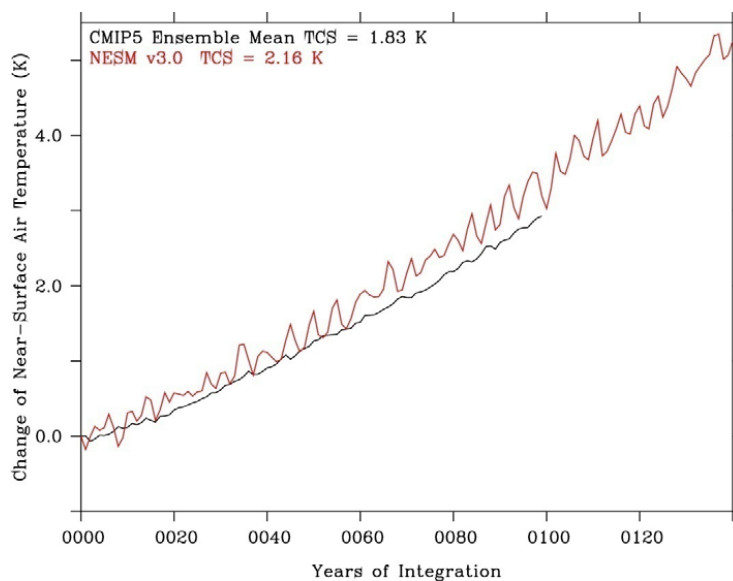
1074

1075

1076

1077

1078



1079

1080 Figure 14 Results from the 1%per year CO₂ increases experiment. Global mean annual surface air

1081 temperature change relative to counterpart in the PI experiment. The red and black lines indicate

1082 the results obtained from the NESMv3 and 10 CMIP5 models' MME, respectively. The average

1083 temperature anomalies between year 60-80 is defined as transit climate sensitivity, which is

1084 2.16K in the NESM v3 model.